Residual stress and cracking in expanded austenite layers

2005 J. Phys.: Condens. Matter 17 3547

(http://iopscience.iop.org/0953-8984/17/23/007)

INSTITUTE OF PHYSICS PUBLISHING JOURNAL OF PHYSICS: CONDENSED MATTER

J. Phys.: Condens. Matter **17** (2005) 3547–3558 doi:10.1088/0953-8984/17/23/007

Residual stress and cracking in expanded austenite layers

D Hoeft[1,2], B A Latella[2,3] and K T Short[2]

[1] University of Bremen, Fachbereich Produktionstechnik, Bremen, Germany
[2] Materials and Engineering Science, Australian Nuclear Science and Technology Organisation, Private Mail Bag 1, Menai, NSW 2234, Australia

E-mail: bal@ansto.gov.au (B A Latella)

Received 15 March 2005, in final form 29 April 2005
Published 27 May 2005
Online at stacks.iop.org/JPhysCM/17/3547

Abstract

The residual stress state and mechanical properties of an expanded austenite layer produced by plasma immersion ion implantation (PI^3) on type 316 austenitic stainless steel substrates at different temperatures were investigated. Residual stress data were obtained using the substrate curvature technique for six different treatment temperatures in the range 360–520 °C. Lattice expansion, nitrogen concentration with depth and mechanical properties of the layer were investigated using x-ray diffraction (XRD), glow discharge optical emission spectroscopy (GDOES) and nano-indentation, respectively. Layer strength and fracture toughness behaviour were investigated using tensile testing with optical microscopy to study the cracking evolution *in situ*. The results showed that for the treatments at 360–420 °C lattice expansions greater than 8% were achieved with nitrogen concentrations near 40 at.%. Two distinct stress–temperature regions were identified from the curvature measurements: (i) for treatment temperatures less than 450 °C, high compressive residual stresses in the range 2–3 GPa were found and the fracture resistances of these layers were less than 7 MPa $m^{1/2}$, and (ii) for treatment temperatures above 450 °C, the residual stress was significantly lower (≈0.7 GPa) but remained constant and the fracture toughness of the layer was improved by a factor of two.

1. Introduction

The implantation and diffusion of nitrogen into the surface of austenitic stainless steel using the plasma immersion ion implantation (PI^3) technique can result in a layer with increased hardness and wear resistance without compromising corrosion behaviour. This modified or 'expanded austenite' layer is a metastable and supersaturated unit cell that can have a nitrogen

[3] Author to whom any correspondence should be addressed.

concentration greater than 20 at.% and lattice expansions of up to 12% [1–4]. Yet the exact structure of the layer is not fully understood. Current opinion is that it is not a cubic cell but has a tetragonal distortion [3, 5]. X-ray diffraction (XRD) analyses show that the (200) planes expand the most [3, 4, 6].

Importantly, the expanded lattice constant of the layer and the difference in the thermal expansion coefficient of the expanded layer and the substrate result in significant compressive residual stresses [4, 7]. These high stresses are believed to enhance the properties, namely the hardness and fracture toughness. Generally, compressive surface stresses are introduced, e.g. with shot peening, to improve fatigue and crack resistance, but if excessive they can also cause adhesion failure of a coating [8, 9]. To avoid premature component failure it is important to know the nature and magnitude of residual stress.

Residual stresses can be measured using a variety of techniques, such as the curvature method, hole drilling and XRD or neutron diffraction [9]. Commonly, the non-destructive methods of substrate curvature and XRD are applied for layers and coatings, but in the case of expanded austenite the stress free lattice constant is unknown and therefore a precise stress calculation is difficult from XRD alone. In addition, a chemical shift resulting from the nitrogen concentration complicates matters further. In this work we use the substrate curvature method to minimize these problems. Furthermore, it has some advantages over diffraction techniques. First, the stress calculated from the curvature technique is an average over the whole thickness of the layer. As a result, the microstructural factors of grain size and texture have no discernible effect on the results from the curvature technique. Second, and most importantly, the residual stress in the thin layer can be calculated without knowing the elastic constants of the coating [10].

Accordingly, the objectives of this work were to process expanded austenite layers at various temperatures and examine the residual stress state and the chemical and mechanical properties of the layers. To characterize these properties, substrate curvature, XRD, GDOES and nano-indentation were used. The strength and crack resistance behaviour of the expanded austenite layer using small 'dogbone' samples were investigated using *in situ* optical tensile tests.

2. Experimental method

2.1. Material and treatments

All specimens used were austenitic type 316 stainless steel with the following composition: Cr 16.4%, Mn 2.1%, Fe 68.5%, Ni 10.4% and Mo 2%. For each treatment a pair of a thin square and a dogbone was treated. The square samples were 19×19 mm^2 with a thickness 0.89 mm. The dogbones were the same thickness and total length of 33 mm with a gauge length of 12 mm and width of 3 mm along the gauge. These were punched out using a press from a die assembly. Prior to the implantation process all specimens were polished to a 1 μm finish using a Struers RotoPol machine. To analyse the surface layer, optical and scanning electron microscopy (SEM) were used. Metallographic cross sections of the PI^3 treated samples were etched using Marble's reagent (4 g $CuSO_4$, 20 ml HCl, 20 ml H_2O) to highlight the treated layer.

To achieve approximately equal layer thickness for each treatment temperature, the process times were varied based on previous experiments [3]. Treatments were performed at six different temperatures in the range of 360–520 °C for process times between 960 and 90 min, as listed in table 1. All PI^3 treatments were done using a pure N_2 rf generated plasma, at a working pressure of 15 μbar. The samples were pulse biased with -30 kV and the frequency was adjusted to give an estimated constant dose rate of 1×10^{14} N cm^{-2} s^{-1} during each

Table 1. Applied treatment temperatures with corresponding process times calculated with the diffusion coefficient D ($D = h^2/t$, where t is the process time and h the layer thickness).

Treatment temperature (°C)	Calculated diffusion coefficient D ($\mu m^2\ h^{-1}$)	Process time t (min)
360	3	960
380	5	540
420	12	300
430	18	180
460	38	120
520	80	90

treatment. The system base pressure was $<5 \times 10^{-6}$ mbar, and an Ar/H_2 plasma pre-clean was performed during heating up to the set temperature similar to that reported in [11].

2.2. *Physical characterization*

Phase information was determined by standard Bragg–Brentano geometry XRD on a Phillips 1050 diffractometer with Cu Kα radiation ($\lambda = 1.5406$ Å) to measure the lattice constant of the expanded layer.

Nitrogen depth profiles were obtained by glow discharge optical emission spectroscopy (GDOES) using a LECO GDS-850A system. Argon ions, excited by a DC voltage of 700 V and 20 mA, were used to sputter the upper surface layer and produce a crater of 20 μm depth with a 4 mm diameter. The displaced matter was analysed simultaneously by dual emission spectrometers, creating an elemental depth profile. For ease of measurement 3 mm thick treated stainless steel samples ($19 \times 19\ mm^2$) were also tested and the results were found to be comparable to the equivalent thin materials used throughout this work.

The curvature was measured with a Tencor Alpha-Step 200 stylus profilometer with a scan length of 10 mm. Measurements were performed in both orientations (x and y directions) along the midpoint of the square samples. The average curvature was then used to compute the corresponding stress. Equation (1) shows the relationship between the change in the radius of curvature of a treated and untreated sample and the corresponding residual stress in the layer [12]:

$$\sigma_r = \frac{1}{6}\left[\frac{1}{R_{post}} - \frac{1}{R_{pre}}\right]\frac{E_s}{(1-\nu)}\frac{t_s^2}{t_f} \tag{1}$$

where R_{pre} is the radius of curvature before treatment, and R_{post} after treatment, E_s and ν are the modulus ($E_s = 210$ GPa) and Poisson's ratio ($\nu = 0.3$) of the substrate, t_s the substrate thickness and t_f the layer thickness. Assuming that the scan length L of the sample is much greater than the final bow, B, of the wafer, the radius, R, can be calculated using

$$R = \frac{L^2}{8B}. \tag{2}$$

Based on the force balance on the cross section of the substrate the internal residual strain, ε_r, can be expressed as

$$\varepsilon_r = \frac{\sigma_r}{E_f} \tag{3}$$

where σ_r is the internal residual stress in the layer and E_f the layer modulus (valid for a plane stress field with $\sigma_{xx} = \sigma_{yy} = \sigma$, $\sigma_{zz} = 0$).

2.3. Mechanical characterization

The hardness and Young's modulus of the layer were investigated using an Ultra Micro-Indentation System (UMIS 2000, CSIRO, Australia). For indentation a diamond Berkovich (three-sided pyramid) tip was used. The applied maximum loads used were in the range of 50–150 mN. For each load at least three indentations were made with a spacing of 20 μm and the results averaged. Further details of the method can be found in [13].

Examination of cracking evolution in the expanded austenite layer as a result of an applied tensile force was made using a small testing device [7]. During the tests a load cell recorded the force and a linear variable displacement transducer the imposed displacement. All dogbones were pulled with a constant crosshead speed of 5 μm s^{-1} to a final strain of about 6%. Due to the small size and design of the device it could be placed under an optical microscope (Zeiss AxioTech vario 100, Germany), and the region of interest (which remains essentially stationary) could be observed during the whole testing time and images captured with a camera.

Analysis of the critical stress, σ_c, for cracking of a layer is defined by

$$\sigma_c = \varepsilon_f E_f \tag{4}$$

where ε_f is the strain for the first cracking observed in the layer and E_f the modulus of the expanded austenite layer. The stress state of the layer is then the sum of the stress induced by straining the system and the internal residual stress. The critical stress σ_c for cracking in the layer is then given by

$$\sigma_c = (\varepsilon_f + \varepsilon_r) E_f \tag{5}$$

with ε_r for the residual strain obtained from the curvature measurement. In the case of compressive stress the residual strain is negative. Once the critical strain is reached the layer begins to crack and the intercrack spacing decreases with increasing applied strain until crack saturation is reached, yielding a minimum crack spacing.

The resistance of the material to cracking is the fracture toughness K_{IC}, which can be determined from the following [14, 15]:

$$K_{IC} = \left(\sigma_c^2 t_f \left[\pi F(\alpha_D) + \frac{\sigma_c}{\sqrt{3}\sigma_y} \right] \right)^{1/2} \tag{6}$$

where σ_c is the critical stress, t_f is the layer thickness, σ_y is the yield stress of the substrate (obtained from the tensile experiment) and $F(\alpha_D)$ is a function of the elastic contrast between layer and substrate [16].

To investigate these properties for layer/coating on substrate systems, the layer must be brittle and perfectly adhered to a ductile substrate, so that the displacement/deformation of the substrate is entirely transmitted to the layer through the interface. In this work the adhesion is considered near perfect as the layer is grown from the substrate.

3. Results and discussion

Representative XRD traces are shown in figure 1(a) for the untreated stainless steel and the expanded austenite layer after the 420 and 520 °C treatments. The patterns have been offset for clarity. The XRD plot of the untreated austenitic stainless steel shows the major austenite peaks (denoted γ_{hkl}) for the (111), (200), (220) and (311) reflections. The corresponding patterns for the treated samples show the expanded austenite peaks (denoted $\gamma_{N(hkl)}$) that have been shifted to smaller 2θ angles indicative of lattice expansion. It is important to note that the peak shifts observed are not linear with respect to the diffraction angle but for equivalent reflections are noticeably greater in extent for the 420 °C compared to the 520 °C treated

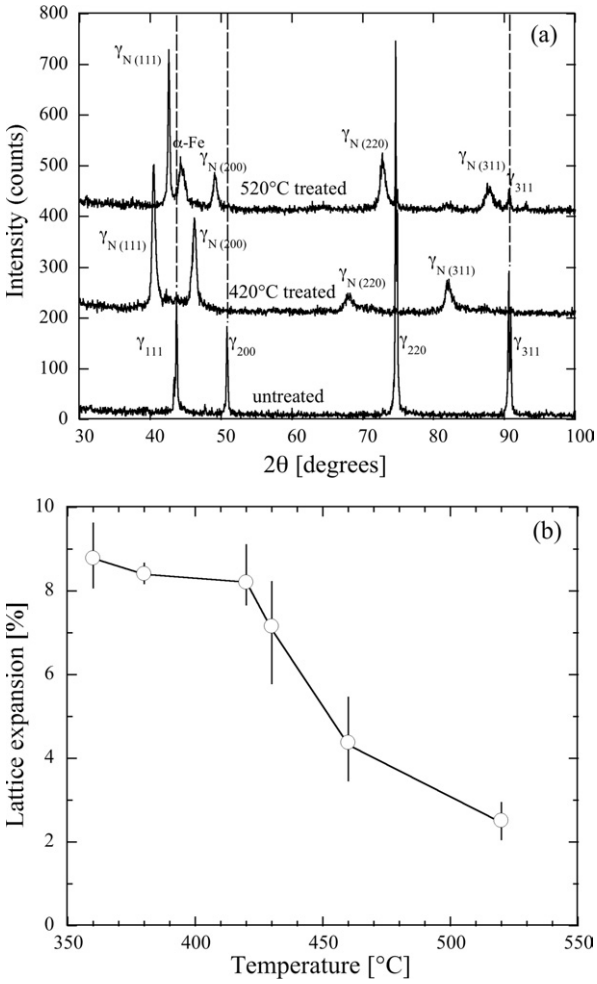

Figure 1. (a) Comparison of XRD patterns showing untreated, 420 and 520 °C treated samples. The x-ray spectra are offset for clarity. The peaks are labelled either γ_{hkl} for the untreated and $\gamma_{N(hkl)}$ for the treated where $hkl = 111$, 200, 220 or 311. The dashed lines are used for comparison purposes to show the reflection peak positions of the untreated stainless steel and the expanded austenite. (b) Average lattice expansion for the (111), (200), (220) and (311) planes as a function of treatment temperature. The bars delineate the range in the computed lattice expansion values for the four reflections.

material. Similarly the increased peak height of the (111) reflections dominate the x-ray spectra in expanded austenite compared to that in the untreated, so that the layer exhibits texture (preferred orientation), and together with the (200) plane show the greatest expansion in agreement with previous studies [3, 6, 17]. The texturing towards the (111) plane may be a consequence of the plane specific elastic modulus in fcc metals [17, 18]. The 520 °C pattern shows the presence of α-Fe (ferritic in nature) but there is no evidence of CrN peaks, which is due to the relatively short treatment time and the fine-grained cold-rolled stainless steel sheet used. The formation of CrN becomes prevalent at these temperatures when longer processing times ($\geqslant$3 h) are used, from which thicker expanded austenite layers are produced [3, 7].

Figure 1(b) shows the matching percentage expansion of the original fcc austenite cell due to the diffusion of nitrogen atoms into the interstitial lattice spaces for all applied treatments.

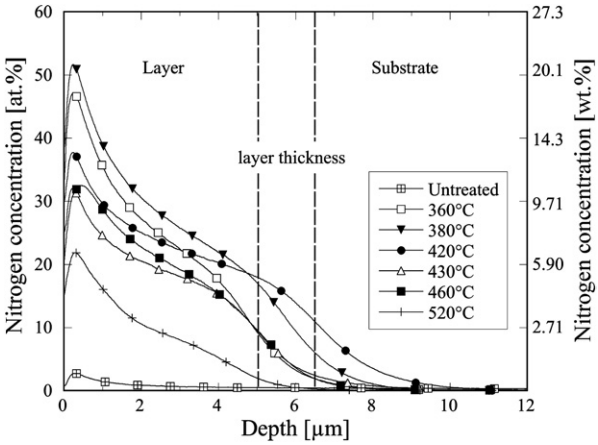

Figure 2. Nitrogen concentration depth profiles for all treatments obtained from GDOES. Dashed lines indicate the spread in layer thickness computed from SEM images for all treatment temperatures.

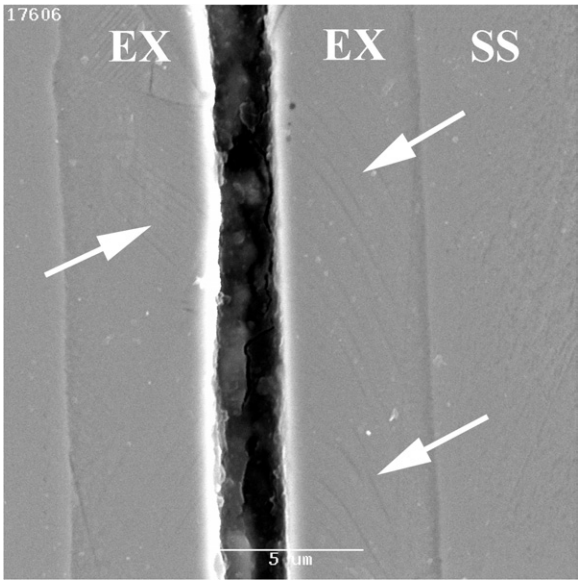

Figure 3. SEM image of cross sections showing the expanded austenite layer (EX) for the 360 °C treatment along with the abrupt interface with the stainless steel (SS). Arrows point to several major slip lines within the layer, indicating plastic flow. Sample etched using Marble's reagent.

The data points are the average values for the (111), (200), (220) and (311) planes. The error bars indicate the range in the percentage expansion calculated for each of the four peaks used in the analysis. At low temperature and long treatment times the average expansion is approximately 8.5%; at high temperatures it decreases with increasing temperature to an expansion of 2.1%. Additionally, the expansion varies with the lattice direction of the unit cell (as illustrated in figure 1(a)), an outcome of which is the discernible variability in the data.

The nitrogen concentration depth profiles (in at.%) for all treatments are shown in figure 2 along with the untreated stainless steel for comparison. The shaded band depicts the layer

Table 2. Layer thickness, indentation hardness and Young's modulus for each treatment temperature. Hardness and Young's modulus values determined from nano-indentation tests with maximum load of 100 mN.

Treatment temperature (°C)	Layer thickness t_f (μm)[a]	Hardness (GPa)	Young's modulus E_f (GPa)
Untreated	—	2 ± 0.2	210 ± 2[b]
360	5.5 ± 0.2	14 ± 2.8	227 ± 19
380	6.4 ± 0.2	15 ± 0.8	225 ± 12
420	7 ± 0.2	17 ± 3.8	260 ± 27
430	5 ± 0.2	13 ± 0.9	220 ± 5
460	5 ± 0.2	10 ± 1.5	209 ± 11
520	4.6 ± 0.2	6.6 ± 0.3	190 ± 3.5

[a] Layer thickness measurements obtained from SEM images.
[b] Determined using the impulse excitation technique [26].

thickness range determined from SEM images (refer to figure 3 and table 2). For the 360 and 380 °C treatments the nitrogen concentration is between 40 and 50 at.% for the first 100 nm in depth. The nitrogen concentration progressively decreases with increasing treatment temperature to a level of about 20 at.% at 0.1 μm depth for the 520 °C treatment. The characteristic peak at about 0.25 μm depth in the profiles of all treatments may be due to the implantation kinetics dominating at this depth over diffusion, although the peak should be reduced at higher temperatures, where diffusion is much faster. Another possibility is adsorption of atmospheric nitrogen into the surface, which is certainly the case for the untreated material.

The GDOES profiles do not show a distinct interface region by virtue of the technique having a depth resolution of about 15%. By comparison, a representative SEM image given in figure 3 shows an abrupt interface between layer and substrate for the 360 °C treated material. From SEM the average layer thickness for all treatments was found to be 5.6 ± 0.9 μm. Stylus profilometry has shown that the sputtered craters produced have a concave profile, indicating poorer depth resolution at higher depths, which is evident by the extensive tailing in the GDOES curves. The highest N depth measured was obtained for the 420 °C treatment.

The hardness and Young's modulus of the treated materials as determined by nano-indentation are listed in table 2. The layer hardness for all treatments exhibit an increase between 650% and 850% compared to the untreated stainless steel. The 420 °C treatment exhibits the highest hardness and Young's modulus of 17 and 260 GPa, respectively. The variations in hardness and Young's modulus remain relatively high for the 360–430 °C treatments but there is a perceptible decline in these properties for the 460 and 520 °C treatments. The effect of differing layer thickness and substrate influences on the nano-indentation measurements were essentially minimized by judicious choice of the loads used and the penetration depths obtained, i.e. the indentation depths ranged from ≈490 nm (7% of layer thickness) in the 420 °C material to ≈760 nm (17% of layer thickness) for the 520 °C material at a load of 100 mN [19].

Caution is needed in interpreting the Bragg–Brentano XRD patterns of these layers, as the method only gives the interplanar lattice spacing for those planes oriented parallel to the surface. Information from grains with crystallographic planes oriented in any other directions is neglected in this configuration. The lattice expansion is determined by comparing the peak positions for the expanded austenite layer to the bulk unstrained stainless steel. The sources of anisotropic lattice expansions observed by XRD are a result of the superposition of (i) chemical shift effects in the layer due to variations in the N concentration with crystal orientation, (ii) the

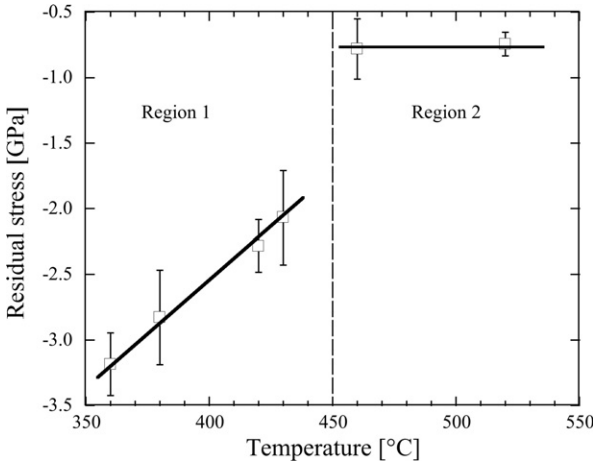

Figure 4. Intrinsic residual stress as a function of the treatment temperature. Note that negative stress values signify that the expanded austenite layer is in compression. A dashed vertical line delineates the two regions.

implantation and in-diffusion of N process, as intergranular strains, and (iii) thermal strains due to differential thermal contraction of the material on cooling from the treatment temperature. This indicates that meaningful residual stress calculations using the method are complicated at best. Clearly, if the effects of chemistry and the residual stresses induced can be separated then significant information can be extracted for the expanded austenite layer. Furthermore, the stress is expected to vary with depth and it is unknown which type of stress (micro or macro [20]) dominates from the XRD analysis performed. Accordingly, the curvature method is used to circumvent the problems and issues outlined to give a global average measure of the residual stress in the expanded layer as described below. However, at the level of the grain scale, intergranular stresses within certain regions of the layer may exceed the macroscopic average residual stress measured in this study.

The residual stress results from the substrate curvature measurements are shown in figure 4. For the lower temperature treatments the residual stress is about −3 GPa. At 430 °C the stress is about −2 GPa and drops to −0.7 GPa for the high temperature treatments. The generally lower N concentrations and lower lattice expansion (<4%) generate weaker compressive stresses within the layer at the higher temperatures. As a result the residual stress versus treatment temperature data in figure 4 can be divided into two distinct regions: Region 1 (for temperatures <450 °C) shows a linear decrease in compressive stress with rising temperature; for region 2 (temperatures >450 °C) a plateau in the stress is observed, indicating a definite saturation level.

The high number of defects, visible by electron microscopy within these layers (figure 3), suggests the onset of plastic flow during the implantation process. This intimates that the yield strength of the expanded austenite layer may be exceeded at these temperatures, limiting the stress induced to a threshold value and a reduction with increasing time due to stress relief [4]. In order to gain an insight into the yielding/relief process a simple calculation can be performed based on knowledge that the yield strength of a material equals approximately one-third of the indentation hardness [21, 22]. Hence at temperatures of ≈400 °C the hardness is about 40% of the ambient temperature value [23], so for the 380 and 420 °C treatments (see table 2) the yield stress computed is in the range 2–2.3 GPa. This is the same order of magnitude and is near the residual stress values measured from the curvature experiments, indicating that material flow

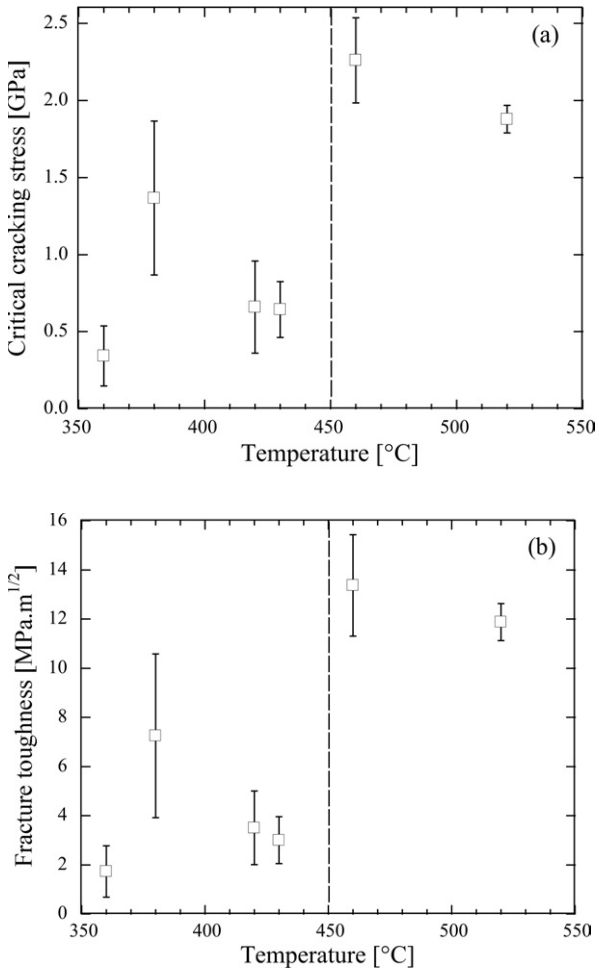

Figure 5. (a) Critical stress for cracking and (b) fracture toughness of the expanded austenite layer as a function of treatment temperature. The dashed vertical line delineates the two regions identified in figure 4.

is likely. Transmission electron microscopy studies have also demonstrated a region of high dislocation density at the boundary with the underlying substrate [3, 5].

From the stress data plotted in figure 4, the residual strains may be calculated using equation (3), from which the corresponding lattice expansions obtained range from 0.37% to 1.4%. Compared to the lattice expansion data given in figure 1(b) these shifts due purely to stress in the layer are quite low. It is readily apparent that the major component of the peak shifts observed in figure 1(a) is due to the N concentration. Even with this knowledge, deconvoluting the chemical and stress effects in XRD measurements due to the anisotropic peak shifts remains unanswered and is beyond the scope of this work.

The critical stress for cracking and the fracture toughness, K_{IC}, of the expanded austenite layer as a function of temperature are shown in figures 5(a) and (b), respectively. The critical point when the layer begins to crack due to the applied load corresponds to the maximum tensile stress the layer can withstand before rupture, i.e., the strength of the layer. For the treatments at $<450\,^{\circ}$C even though the stress is high the strength is relatively low, due to the plastic

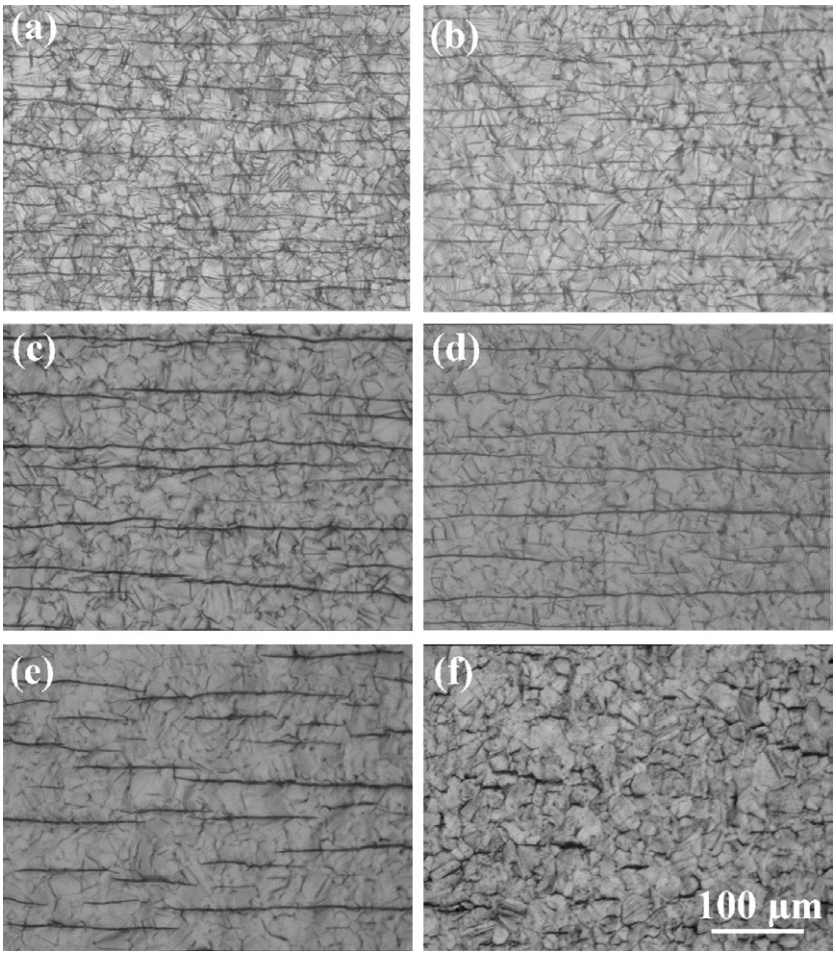

Figure 6. Sequence of optical micrographs showing the damage observed in the expanded austenite layers after tensile loading to a final strain of about 6% for (a) 360 °C, (b) 380 °C, (c) 420 °C, (d) 430 °C, (e) 460 °C and (f) 520 °C treatment. Tensile loading applied is in the vertical direction for the images shown.

deformation at temperature and high defect density that resulted as shown in the SEM cross-sections (figure 3). For the 460 and 520 °C treatments the strength was increased considerably, pointing to a distinct transition in mechanical response akin to the stress behaviour. The fracture toughness data showed the same trend with $K_{IC} = 1$–7 MPa $m^{1/2}$ for treatment temperatures less than 450 °C and ≈14 MPa $m^{1/2}$ above 450 °C. Generally, it would be expected that higher compressively stressed layers would exhibit improved toughness, but this is not the case. For comparison, typical steels have a K_{IC} about 50 MPa $m^{1/2}$. Clearly, the defect density plays a major role in the strength and toughness response of the expanded austenite layer, but not so for hardness. Moreover, the magnitude of the stress induced controls the hardness and appears to govern the number of defects, which directly influences the critical cracking stress.

Figure 6 shows the optical images for all treatments at final tensile strain of 6%. The prominent feature in the majority of the images is the regular spacing of typically long parallel cracks perpendicular to the loading axis (here the loading applied is vertical in plane of all

the images). Grain boundary junctions and defects were the main sources of the nucleation of these cracks from the *in situ* optical microscopy viewing. The cracking damage in expanded austenite is similar to that shown in initial work on this system [7] and is also a feature of hard coatings deposited on metallic substrates [13, 24, 25]. The observed cracking behaviour of the expanded layer at lower temperatures shows that the intercrack spacing is $\approx$12 μm for the 360 and 380 °C (figures 6(a) and (b)) and $\approx$21 μm for the higher temperatures (figures 6(c) and (d)). In the 460 °C material (figure 6(e)) the parallel cracks are reduced in length and extent and for the 520 °C treatment (figure 6(f)) no long parallel cracks through the layer can be observed, but only small microcracks at some grain boundaries, indicating improved toughness. For all treatments no decohesion of the layer from the substrate has been observed, which indicates the excellent bonding of the layer to the substrate.

Irrespective of the cracking damage the grain structures of the layers show differing degrees of twinning and slip lines which result from the treatment. The images of the low temperature treatments, particularly the 360 and 380 °C (figures 6(a) and (b)), show significantly more deformation in the form of twinning, which again supports evidence of plastic deformation occurring at temperature. Further, the level of deformation observed in the microstructures of the layer for each treatment, which are generally equivalent in grain size, seem to play a crucial role in the differences observed in the strength and toughness data in figure 5.

4. Conclusion

The dependency of residual stress on treatment temperature using PI^3 on stainless steel 316 has been shown. Low temperature treatments (<450 °C) cause high lattice expansions up to 8% with over 20 at.% of nitrogen in the surface region which leads to relatively high compressive residual stress of 3 GPa. These internal stresses are higher than the yield strength of the produced expanded austenite layers, which caused plastic flow in the outer surface region. Distinct regions of the induced stress and mechanical property behaviour were observed and defined. For temperatures <450 °C a linear decrease in compressive stress with rising temperature was noted, whereas above this temperature a constant stress of around -0.7 GPa was attained. The transitions in mechanical response were most evident in the optical microscope images of the multiple crack-damaged layers. The high defect density in these layers, particularly for the lower treatment temperatures, resulted in reduced strength and resistance to cracking. This was attributable to the high stresses induced by the implantation process, which is likely to cause deformation and piled-up slip lines given that the magnitudes of the stresses are equivalent to the yield stress of the layer. These defects act as a potential site for cracking in the layer when loaded in tension. The results show that with higher nitrogen concentration the layer is more brittle, with higher crack density observed from tensile testing and lower fracture toughness.

Acknowledgments

The authors would like to thank J Davis (ANSTO) for assistance with SEM and P C King (Deakin University) for performing the GDOES measurements.

References

[1] Collins G A, Hutchings R, Short K T, Tendys J, Li X and Samandi M 1995 *Surf. Coat. Technol.* **74/75** 417
[2] Blawert C, Weisheit A, Mordike B L and Knoop F M 1996 *Surf. Coat. Technol.* **85** 15

[3] Fewell M P, Mitchell D R G, Priest J M, Short K T and Collins G A 2000 *Surf. Coat. Technol.* **131** 300
[4] Sienz S, Mändl S and Rauschenbach B 2002 *Surf. Coat. Technol.* **156** 185
[5] Mitchell D R G, Attard D J, Collins G A and Short K T 2003 *Surf. Coat. Technol.* **165** 107
[6] Blawert C, Kalvelage H, Mordike B L, Collins G A, Short K T, Jiraskova Y and Schneeweiss O 2001 *Surf. Coat. Technol.* **136** 181
[7] Latella B A and Short K T 2004 *J. Mater. Sci.* **39** 4321
[8] Perry A J, Sue J A and Martin P J 1996 *Surf. Coat. Technol.* **81** 17
[9] Withers P J and Bhadeshia H K D H 2001 *Mater. Sci. Eng.* **17** 355
[10] Wang Q, Ishikawa H, Nakano S, Ogiso H and Akedo J 2004 *Vacuum* **75** 225
[11] Menthe E and Rie K-T 1999 *Surf. Coat. Technol.* **116–119** 199
[12] Stoney G G 1909 *Proc. R. Soc.* A **82** 172
[13] Latella B A, Gan B K, Davies K E, McKenzie D R and McCulloch D G 2005 *Surf. Coat. Technol.* at press
[14] Ignat M, Marieb T, Fujimoto H and Flinn P A 1999 *Thin Solid Films* **353** 201
[15] Atanacio A J, Latella B A, Barbé C J and Swain M V 2005 *Surf. Coat. Technol.* **192** 354
[16] Beuth J L and Klingbeil N W 1996 *J. Mech. Phys. Solids* **44** 1411
[17] Mändl S and Rauschenbach B 2000 *J. Appl. Phys.* **88** 3323
[18] Korsunsky A M, James K E and Daymond M R 2004 *Eng. Fract. Mech.* **71** 805
[19] Fischer-Cripps A C 2002 *Introduction to Nanoindentation* (New York: Springer)
[20] Withers P J and Bhadeshia H K D H 2001 *Mater. Sci. Eng.* **17** 366
[21] Ashby M F and Jones D R H 1996 *Engineering Materials 1: An Introduction to Their Properties and Applications* 2nd edn (Oxford: Pergamon)
[22] Davies K E, Gan B K, McKenzie D R, Bilek M M M, Taylor M B, McCulloch D G and Latella B A 2004 *J. Phys.: Condens. Matter* **16** 7947
[23] Rothman M F (ed) 1988 *High-Temperature Property Data: Ferrous Alloys* (Metals Park, OH: ASM International)
[24] Scafidi P and Ignat M 1998 *J. Adhes. Sci. Technol.* **12** 1219
[25] Latella B A, Ignat M, Barbé C J, Cassidy D J and Bartlett J R 2003 *J. Sol–Gel Sci. Technol.* **26** 765
[26] Latella B A and Humphries S R 2004 *Scr. Mater.* **51** 635